

SLoRD: Structural Low-Rank Descriptors for Shape Consistency in Vertebrae Segmentation

Xin You, Yixin Lou, Minghui Zhang, Jie Yang, Nassir Navab*, *Fellow, IEEE*, Yun Gu*, *Member, IEEE*

Abstract—Automatic and precise multi-class vertebrae segmentation from CT images is crucial for various clinical applications. However, due to a lack of explicit consistency constraints, existing methods especially for single-stage methods, still suffer from the challenge of intra-vertebrae segmentation inconsistency, which refers to multiple label predictions inside a singular vertebra. For multi-stage methods, vertebrae detection serving as the first step, tends to be affected by the pathology and metal implants. Thus, imprecise detections cause biased patches before segmentation, which then leads to inaccurate contour delineation and inconsistent segmentation. In our work, we intend to label individual and complete binary masks to address that challenge. Specifically, a contour generation network is proposed based on Structural Low-Rank Descriptors for shape consistency, termed SLoRD. For a structural representation of vertebral contours, we adopt the spherical coordinate system and devise the spherical centroid to calculate contour descriptors. Due to vertebrae's similar appearances, basic contour descriptors can be acquired to restore original contours. Therefore, SLoRD leverages these contour priors and explicit shape constraints to facilitate regressed contour points close to vertebral surfaces. Quantitative and qualitative evaluations on VerSe 2019 and 2020 demonstrate the superior performance of our framework over other single-stage and multi-stage state-of-the-art (SOTA) methods. Further, SLoRD is a plug-and-play framework to refine the segmentation inconsistency existing in coarse predictions from other approaches. Source codes are available <https://github.com/AlexYouXin/SLoRD-VerSe>.

Index Terms—Vertebrae segmentation, Inconsistency, Contour descriptors, Refinement

I. INTRODUCTION

Automatic multi-class vertebrae segmentation from CT images plays a significant role in spinal disease treatment, including preoperative diagnosis, surgical guidance, and postoperative assessment [5], [21], [22]. Moreover, the shape analysis of vertebrae serve as an important anatomical reference for other anatomies in clinical practices [9], [28]. According to the anatomical prior of vertebral structures, it is emerging to

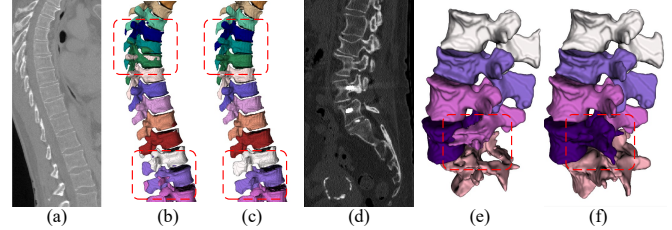


Fig. 1. (a) CT case 1. (b-c) Coarse prediction by 3D UNet & refined outcome by 3D UNet + SLoRD on case 1. (d) CT case 2 with metal artifacts. (e-f) Coarse prediction by the multi-stage pipeline Spine-Transformer [38] & our refined prediction on case 2.

preserve the consistency of label predictions inside a singular vertebra [24]. However, as illustrated in Fig. 1, for single-stage and multi-stage methods, predicted masks for the specific vertebra might contain inconsistent label predictions, and partial voxel predictions in adjacent vertebrae reveal the same label. That phenomenon has been recognized as intra-vertebrae label inconsistency [45], which poses an enormous challenge for the task of precise vertebrae segmentation.

Specifically, earlier methods solved vertebrae segmentation from volumetric CT images by employing statistical models [20], active shape models [14], level sets [23], Markov random field [17], [18], graph cuts [3] and machine learning theories [10], [19]. However, those approaches fail to perform well on unseen data due to insufficient generalization ability. Current methods based on deep learning techniques demonstrate a more promising performance for vertebrae image segmentation even with arbitrary field-of-views (FOVs). One category of existing works [11], [15], [45] adopted **single-stage** convolutional or Transformer-based networks for automatic vertebrae segmentation and identification. However, these models suffer from drawbacks of similar appearances between adjacent vertebrae and the patch-based inference paradigm [22], resulting in intra-vertebrae label inconsistency as revealed in Fig. 1(a & b). The other methods [26], [27], [31], [38] designed a **multi-stage** pipeline, which can boost the segmentation performance by reducing the disturbance from neighboring contexts based on the localize-then-segment concept. However, a biased local patch from the detection network due to the inaccurate center regression will enforce inconsistency inside vertebrae, particularly for pathological vertebrae with abnormal shapes or metal implants as illustrated by Fig. 1(d & e). Also, this limitation can be referred to according to the qualitative analysis of experimental results in [38].

This work is supported in part by NSFC under Grant 62373243

X. You is with the Institute of Image Processing and Pattern Recognition, Shanghai Jiao Tong University, Shanghai, China. (Email: sjtu_youxin@sjtu.edu.cn)

Y. Lou, M. Zhang, J. Yang, and Y. Gu are with the Institute of Image Processing and Pattern Recognition, Shanghai Jiao Tong University, Shanghai 200240, China (Email: {jiejieyang, geron762}@sjtu.edu.cn).

N. Navab is the Chair for Computer-Aided Medical Procedures and Augmented Reality, Technical University of Munich, Munich, Germany (Email: nassir.navab@tum.de).

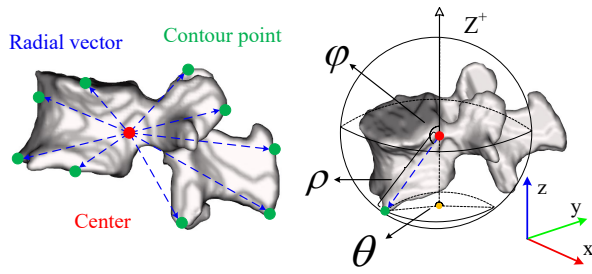


Fig. 2. Spherical coordinate system for 3D vertebral contour descriptions. x , y , and z axis represent voxel orientations from Right/Anterior/Inferior to Left/Posterior/Superior. ρ : the radial distance away from the spherical center, ϕ : the azimuth angle between the radial vector and z^+ , θ : the polar angle between x^+ and the projected radial vector in the XOY plane.

Essentially, all the above methods fail to explicitly impose both contour precision and intra-vertebrae voxel consistency constraints synchronously, resulting in segmentation inconsistency. To resolve this limitation, we attempt to label individual and complete binary masks to achieve multi-label vertebrae segmentation. Due to the connection between superior and inferior articular processes [5], the main challenge is transformed to how to divide joint binary vertebral masks while preserving original contours to the greatest extent [13].

Thus, we devise an effective contour generation network based on Structural Low-Rank Descriptors for shape consistency, termed SLoRD. For the contour representation, the complete point cloud of vertebral boundaries shows an unorganized arrangement with various point numbers. Intuited by [43], we propose a novel way of contour representations based on the spherical coordinate system as shown in Fig. 2. Under that circumstance, structural contour descriptors are efficiently calculated by recording the radial distance. Additionally, spherical centroids are proposed to enhance the precision of contour representations, serving as the spherical center. Then, vertebrae show similar 3D shapes according to anatomical structures, lumbar and thoracic vertebrae in particular. Hence, a low-dimension contour space can be extracted to represent all vertebrae data. Via a linear combination between low-rank basic descriptors in the contour space, instance masks of vertebrae can be approximately restored. Further, vertebral labels provided by coarse predictions facilitate the consistent generation of semantic masks. Ultimately, the whole pipeline is incorporated into SLoRD to boost the framework's generalization abilities on unseen datasets. And the explicit shape constraint and basic contour descriptors are exerted to promote the regression precision of contours. SLoRD serves as a plug-and-play framework, which can repair the segmentation inconsistency from coarse predictions.

Our contributions are summarized as follows: (1) To achieve intra-vertebrae voxel consistency and contour precision simultaneously, we first propose the contour-based generation network named SLoRD, to address the multi-class vertebrae segmentation from CT images with different FOVs. (2) For a structural and efficient contour representation, the spherical coordinate system is adopted to describe the complete contour point cloud. Besides, spherical centroids are devised as the

spherical center to boost the precision of contour representations, based on the anatomical characteristics of vertebrae. (3) Profiting from low-rank basic descriptors in the contour space, regressed contour points will be facilitated close to vertebral surfaces with shape and contour constraints. (4) Extensive experiments on VerSe 2019 and 2020 datasets demonstrate the superior performance of our methods compared with other single-stage and multi-stage approaches, with better segmentation consistency and boundary precision. Moreover, the SLoRD framework serves as a plug-and-play framework to repair intra-vertebrae segmentation inconsistency significantly.

II. RELATED WORK

While the shape of individual vertebrae varies considerably along the spine, adjacent vertebrae still show fairly similar appearances, making them difficult to distinguish [29], [46]. Consequently, the spine presents unique challenges for quantitative image analysis compared to other anatomical structures. Additionally, factors such as pathological appearances, fractures, and metal implant artifacts [45] will introduce further challenges. Earlier studies [1], [2], [16], [36], cannot apply to the segmentation task of CT scans displaying arbitrary FOVs with various label distributions [27], [42]. To resolve these challenges, researchers resort to leveraging anatomical prior knowledge. Relevant research could be roughly categorized into two groups: single-stage and multi-stage frameworks for multi-class vertebrae segmentation.

For single-stage pipelines, Zheng et al. employed nnUNet [15] to perform multi-class vertebrae segmentation. Chang et al. [6] adopted stacked graph convolutional networks by featuring a pre-defined adjacency matrix to encode structural information. However, such approaches fail to model global dependency due to the intrinsic property of convolution [12]. Thus, Verteformer [45] was devised by fusing local details and global contexts with two parallel Transformers. And an edge detection block was proposed to refine intra-vertebrae boundaries. Nevertheless, it is still plagued by similar shapes between adjacent vertebrae and the patch-based inference paradigm, leading to intra-vertebrae segmentation inconsistency. Lessmann et al. [22] used fully convolutional networks by iteratively analyzing image patches for automatic vertebrae segmentation and identification. However, this method relies on the perfect prediction for the first label and hardly recovers from failures in the top vertebra.

In contrast, multi-stage approaches reveal more promising segmentation performance owing to the additional guidance, such as the heatmap and box-based localization of vertebrae. Sekuboyina et al. [34] proposed an interactive spine processing framework, consisting of spine detection by a light-weight network, vertebra labeling based on Btrfly Net [35], and vertebral segmentation by 3D UNet [11]. Payer et al. [31] implemented a three-step approach to first localize the spine, then simultaneously locate and identify each vertebra, and finally segment each vertebra. Besides, Tao et al. [38] introduced a Transformer to handle the labeling task, then employed UNet with the original CT and an auxiliary heatmap as inputs to segment all vertebrae. Chen et al. [7] devised a

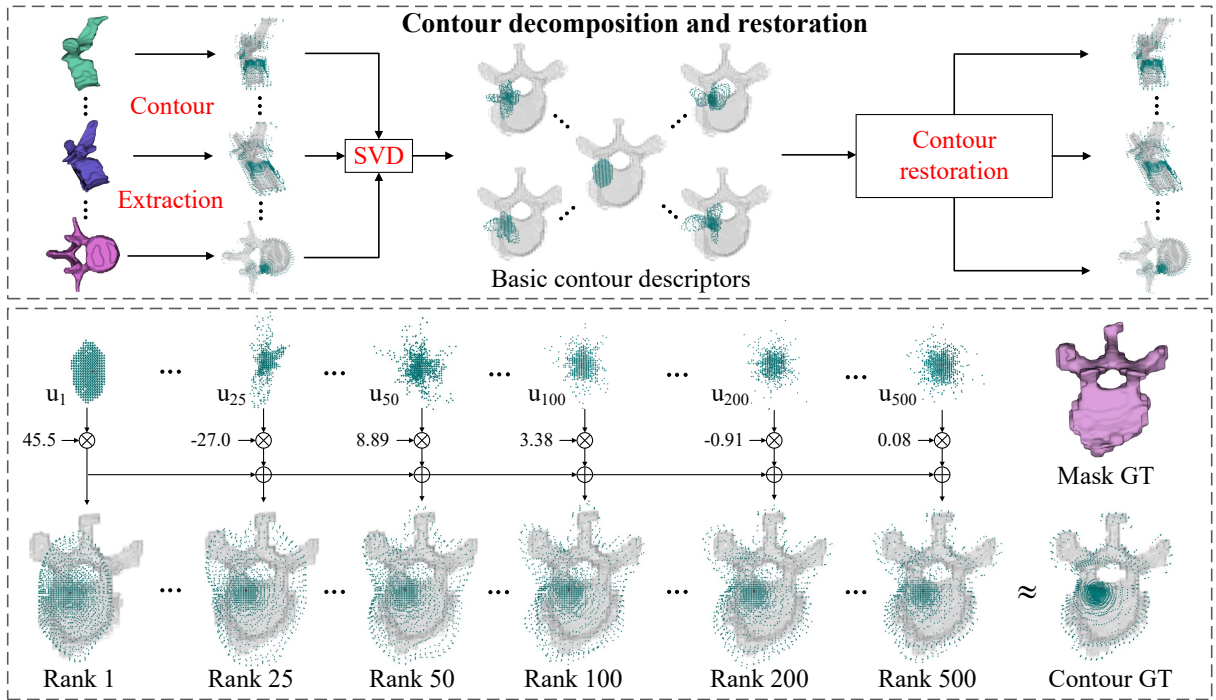


Fig. 3. Upper: The flow of contour decomposition and restoration. Lower: The linear combination process between basic contour descriptors. The first row indicates basic descriptors of specific ranks. The second row refers to weighted visualizations.

deep reasoning module leveraging anatomical prior knowledge to achieve anatomically correct results regarding the sequence of vertebrae. However, the multi-stage pipelines are prone to accumulating errors. An imprecise detected patch with inaccurate center regression will degrade the segmentation performance, particularly for pathological vertebrae with abnormal shapes or metal implants. As a result, the poor contour delineation will enforce inconsistency inside vertebrae.

III. METHODOLOGY

To simultaneously impose the voxel consistency and contour precision regularizations, we propose SLORD by labeling sequential and complete binary masks to achieve multi-class vertebrae segmentation. Specifically, a spherical-based representation mode and spherical centroid are devised for structural and efficient contour representations as described in Section III-A and III-B. Section III-C provides the details of SLORD, which generates precise contour points based on explicit basic descriptors and contour regularization. The pipeline of the inference stage is illustrated in Section III-D.

A. Spherical-based Contour Descriptors

Although the number of contour points varies across different vertebrae, a fixed number of sampling points is required for contour representations. However, it is quite tricky to sample contour points uniformly while maintaining the potential to restore the original contour. Thus, we incorporate the idea from PolarMask [30], [43], in which each contour point is encoded with the polar coordinate. Given the difficulty in extending the polar system to contour representations of 3D objects

like vertebrae, we formulate contours with the spherical coordinate system as shown in Fig.2. Conditioning the inner centroid as the spherical center, we describe the boundary using spherical coordinates $(\rho_{ij}, \theta_i, \phi_j)$, $i=1, \dots, I$; $j=1, \dots, J$. Here ρ represents the length of the radial vector from the spherical center to the contour point, ϕ is the azimuth angle between the radial vector and z^+ , θ means the polar angle between x^+ and the projected radial vector in the XOY plane. Angular coordinates θ_i and ϕ_j are sampled uniformly with a sampling interval s , with I equal to $360/s$, J equal to $(180/s+1)$. Thus, given the sampling angle grid, only radial coordinates are recorded to represent the contour:

$$\boldsymbol{\rho} = [\rho_{11}, \dots, \rho_{1J}, \dots, \rho_{I1}, \dots, \rho_{IJ}]^T \quad (1)$$

Here $\boldsymbol{\rho}$ refers to the contour descriptor, with the dimension N equal to $I \times J$. Considering vertebral anatomies with the non-convex shape property, the spherical system chooses the maximum distance at the same angle to strike a balance between precision and computational cost. Since the shapes of most vertebrae are well structured and resembling to each other, low-rank contour descriptors can be exploited in a data-driven manner via Singular Value Decomposition (SVD) [30]. Detailedly, a non-convex contour matrix $\mathcal{M} = [\boldsymbol{\rho}_1, \dots, \boldsymbol{\rho}_L]$ is constructed from L vertebrae in the training data. Then we perform SVD on matrix \mathcal{M} :

$$\mathcal{M} = \mathbf{U} \boldsymbol{\Sigma} \mathbf{V}^T \quad (2)$$

where $\mathbf{U}^{N \times N} = [\mathbf{u}_1, \dots, \mathbf{u}_N]$ and $\mathbf{V}^{L \times L} = [\mathbf{v}_1, \dots, \mathbf{v}_L]$ are orthogonal matrixes and $\boldsymbol{\Sigma}^{N \times L}$ is a rectangular diagonal matrix, consisting of singular values $[\sigma_1, \dots, \sigma_r]$ with r equal to $\min(N, L)$. The best rank- k approximation of \mathcal{M} can be

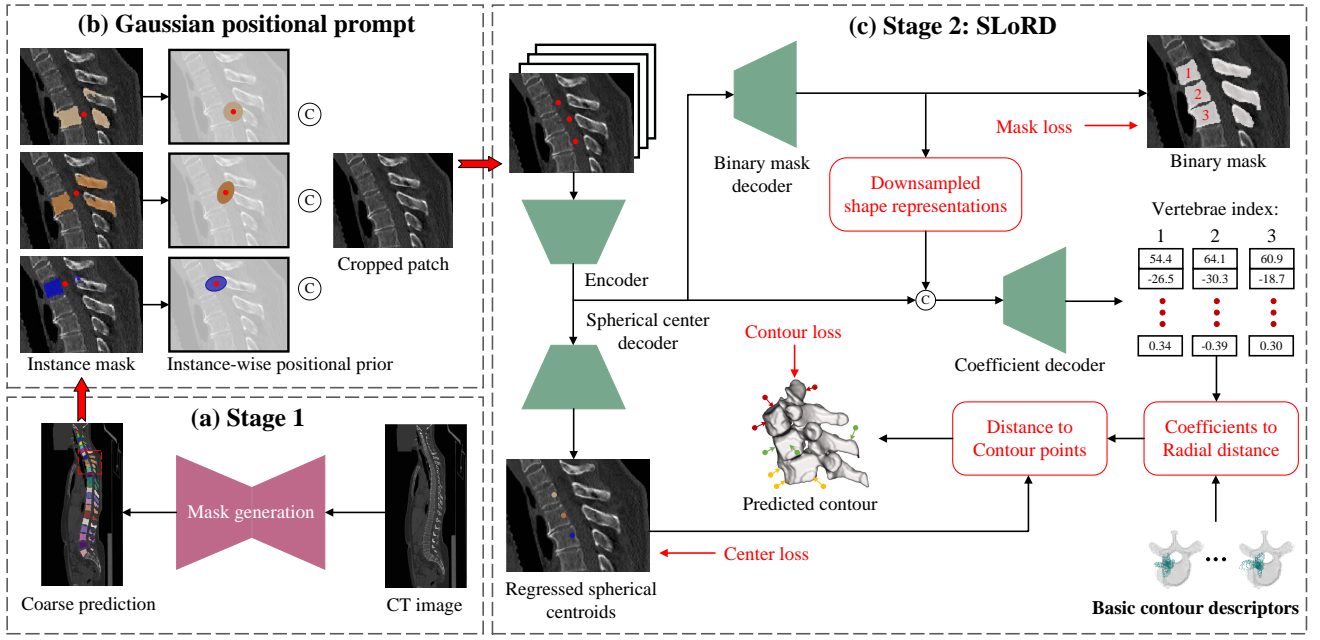


Fig. 4. The two-stage framework. (a) Coarse predictions by arbitrary segmentation networks. (b) The generation of Gaussian positional prompts to boost the center localization precision. (c) Based on the combination of basic contour descriptors, SLoRD aims to regress contour points close to vertebral boundaries via explicit contour and shape regularizations.

calculated as follows:

$$\begin{aligned} \mathcal{M}(k) &= \sigma_1 \mathbf{u}_1 \mathbf{v}_1^T + \dots + \sigma_k \mathbf{u}_k \mathbf{v}_k^T \\ &= [\mathbf{u}_1, \dots, \mathbf{u}_k] \mathcal{C} = \mathbf{U}(k) \mathcal{C} \approx \mathcal{M} \\ \mathcal{C} &= [\sigma_1 \mathbf{v}_1, \dots, \sigma_k \mathbf{v}_k]^T = \mathbf{U}(k)^T \mathcal{M} \end{aligned} \quad (3)$$

Here $\mathbf{U}(k)^{N \times k}$ refers to k basic contour descriptors, which can span into the contour space and be acquired from the training data in advance. $\mathcal{C}^{k \times L}$ means combinational coefficients, calculated by eigen descriptors and matrix \mathcal{M} . As long as \mathcal{C} is correct, we can restore the original contours of vertebrae approximately as illustrated by Fig. 3.

Another relevant research DeepSSM [4], as a shape model based on principal component analysis (PCA), aims to learn the functional mapping from images to low-dimensional latent codes. Then the model achieves discrete contour representations by applying the linear projection on these codes with the PCA basis and mean shape. In comparison, SVD bears the best low-rank approximation properties, and extracted basic descriptors are more robust to fit various anatomical shapes than PCA [40]. Also, the sampling strategy in [4] for the contour point cloud struggles to perform well for pathological vertebral structures with more diverse shapes and topology.

B. Spherical Centroid

Although the encoding scheme for vertebral contours is efficient, it is hard to determine the spherical center, which will significantly affect the restoration performance of vertebral shapes. Since the azimuth angle ϕ and polar angle θ are both sampled at equal intervals, a spherical center with a biased location will result in fewer sampling contour points for the boundary region far from it. Consequently, that region suffers from a contour under-representation. Hence, it has been a crucial topic on how to designate the spherical center.

A simple configuration is each vertebral centroid, averaged on both the vertebral body and spinous process. However, the centroid is acquired ignoring the optimization objective of enforcing contour points close to the boundary \mathcal{B} . Thus, to achieve a finer contour representation for the anatomical structure of vertebrae, a distance-based center should be marked by minimizing the average Euclidean distance between this center and the whole boundary surface. We formulate the distance-based center called spherical centroid C_s based on Eq (4):

$$\begin{aligned} \mathcal{B} &= \mathcal{F}(M) \setminus M \\ C_s &= \arg \min_{c \in M} \left(\frac{1}{|\mathcal{B}|} \sum_{b \in \mathcal{B}} d(c, b) + \lambda \cdot d(c, \delta) \right), \\ \text{s.t. } \delta &= \arg \max_{j \in \mathcal{B}} j_y \end{aligned} \quad (4)$$

where $\mathcal{F}(\cdot)$ represents the morphological dilation operation, M refers to the segmentation mask of each vertebral volume, the boundary map \mathcal{B} is the difference set between the dilated mask $\mathcal{F}(M)$ and the mask itself M . Besides, $d(\cdot)$ means the Euclidean distance. The first item in Eq (4) refers to the average distance from each boundary point b to the center $c \in \mathcal{P}$. Concerning the non-convex shape prior of the spinous process, we attempt to push the spherical centroid closer to it. That will enlarge the value range of θ and ϕ , then enhance the shape representations of the spinous process. That is why the second regularization term is incorporated, in which δ is the boundary point $j \in \mathcal{B}$ with the largest y -dimensional index j_y . λ is a scaling parameter, empirically set as 0.005.

C. Contour Generation with Explicit Contour Priors

To precisely restore the contour with explicit contour descriptors, it is significant to accurately achieve the coefficient according to Eq (3). Besides, the contour generation requires

the precise regression of spherical centers as described in Section III-B. Thus, we devise the SLoRD framework by introducing the center decoder and coefficient decoder as shown in Fig.4(c).

Center decoder: Deep features from the encoder are transformed into regressed spherical centers via combinative operations of convolution, batch normalization, average pooling. The pooling process projects the feature dimension as 3, representing coordinates of the regressed center $\hat{C} = (\hat{c}_x, \hat{c}_y, \hat{c}_z)$. The ground truth of center C_s can be attained by Eq (4). And we employ the L_2 norm to regularize regressed centers \hat{C} , with the center loss \mathcal{L}_{center} equal to $\|C_s - \hat{C}\|^2$. Concerning the limitation that some methods wrongly detect centers of specific pathological vertebrae, we aim to introduce Gaussian positional prompts as additional inputs for positional guidance. As shown in Fig.4(b), the positional prompt is defined as a Gaussian distribution \mathcal{G} based on the follow formula:

$$\mathcal{G}(\mu; \sigma) = \mathcal{G}(\mu_x; \sigma_x) \cdot \mathcal{G}(\mu_y; \sigma_y) \cdot \mathcal{G}(\mu_z; \sigma_z) \quad (5)$$

$$\sigma = \max(m, \bar{m}) / 4, \quad \bar{m} = \frac{1}{L} \sum m \quad (6)$$

Specifically, the mean value $\mu = (\mu_x, \mu_y, \mu_z)$ is set as the centroid based on the coarse prediction. For defining the variance $\sigma = (\sigma_x, \sigma_y, \sigma_z)$, we aim to cover the whole shape distribution using the given \mathcal{G} . Thus, as suggested by the two-sigma rule in mathematical statistics, the length of 4σ should encompass the 3-dimension length $m = (m_x, m_y, m_z)$ of each instance mask. Further, a threshold \bar{m} is introduced to ensure a wide enough region with attention weights decaying from the center μ to the vertebral boundary. The center decoder will modify coarse centroids μ as refined spherical centroids via \mathcal{L}_{center} .

Coefficient decoder: Similar to the center decoder, this part is also a combination of convolution, normalization and average pooling layers, with the projected dimension equal to the rank size. Here a direct loss on combinational coefficients like the previous work [30] cannot work in this task. We reckon that phenomenon results from the magnitude difference between different dimensions of coefficient vectors and the magnitude variance between coefficient vectors at the same dimension. Thus, we transform coefficients into the radial distance with data-driven contour priors, then into the contour point cloud [41] centered at spherical centroids. After that, an explicit contour constraint $\mathcal{L}_{contour}$ is devised based on the average minimal distance from the contour point set \mathcal{P}_c to the boundary interface \mathcal{B} as illustrated by the following formula:

$$\mathcal{L}_{contour} = \frac{1}{|\mathcal{P}_c|} \sum_{p \in \mathcal{P}_c} \min_{b \in \mathcal{B}} d(p, b) \quad (7)$$

where $|\mathcal{P}_c|$ means the voxel number of \mathcal{P}_c . Besides, it might be confusing why a straightforward distance regularization is not conducted on the regressed point clouds. A comprehensible perspective is that SLoRD does not bear any perception ability to identify the sampled angle grid in the spherical coordinate system with no angular priors introduced. That is why basic contour descriptors will boost the contour representation of vertebral anatomies.

Loss term: To reduce computational costs, we uniformly sample $\frac{1}{3}$ boundary points from \mathcal{B} to calculate the contour loss.

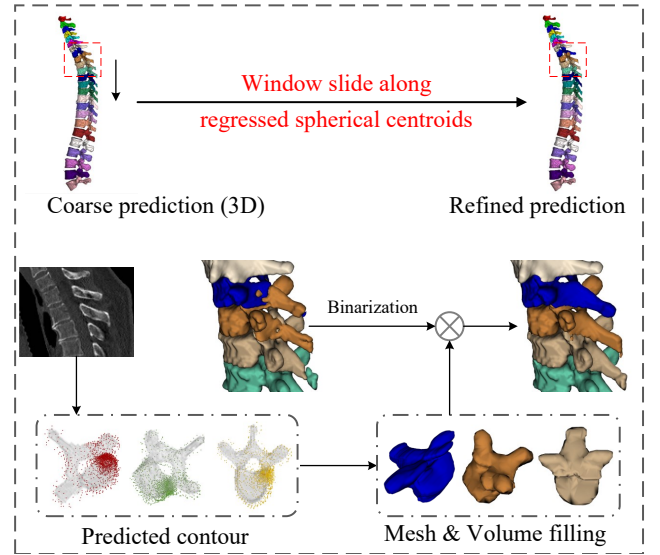


Fig. 5. Iterative refinement for coarse masks in the inference stage.

Besides, an additional binary mask supervision \mathcal{L}_{mask} (cross-entropy + Dice loss) will exert implicit shape information. Thus, the total loss is defined as follows:

$$\mathcal{L} = \mathcal{L}_{mask} + \mathcal{L}_{center} + \mathcal{L}_{contour} \quad (8)$$

Furthermore, segmentation inconsistency tends to appear in a sequence of vertebrae as highlighted in Fig.1. Under this circumstance, the iterative refinement for one vertebra each time cannot well address this type of failure cases, hence we attempt to handle three sequential vertebrae once. Assuming that coarse predictions reveal satisfactory performance for the top two vertebrae, even with a moderate inconsistency, SLoRD can significantly boost segmentation results.

D. Inference

In the inference phase, the patch to be refined in SLoRD is cropped along each vertebral center from coarse predictions as shown in Fig.4(a). The SLoRD framework will first refine three spherical centers corresponding to sequential vertebrae according to the prediction of the center decoder. Then the coefficient branch will output $3 \times N$ (N refers to the dimension of ρ) contour points surrounding three vertebral surfaces with different labels as revealed in Fig.5. After that, Marching Cube [25] is implemented to generate triangle meshes, which are further voxelized into a filled volume [33]. After that, we perform the binarization on the coarse mask and multiply it with the filled volume to realize a refined mask with good label consistency and shape restoration via the auxiliary connected component analysis.

IV. EXPERIMENT

A. Experimental Settings

VerSe 2019 & 2020. To assess the efficacy of our method, we conduct experiments on the Large Scale Vertebrae Segmentation Challenge (VerSe 2019 & 2020) [34]. Specifically, VerSe 2019 consists of 160 spinal CT scans, split into 80/40/40

TABLE I

COMPARISONS WITH OTHER SINGLE-STAGE, TWO-STAGE, AND MULTI-STAGE METHODS ON THE PUBLIC AND HIDDEN TEST DATASETS OF VERSE 2019 (A-DICE: AVERAGE DICE. M-DICE: MEDIAN DICE. A-HD: AVERAGE HAUSDORFF DISTANCE. M-HD: MEDIAN HAUSDORFF DISTANCE).

Stage	Method	Public test				Hidden test			
		A-Dice \uparrow	M-Dice \uparrow	A-HD \downarrow	M-HD \downarrow	A-Dice \uparrow	M-Dice \uparrow	A-HD \downarrow	M-HD \downarrow
Single-stage	3D UNet [11]	81.13	94.71	16.36	13.81	81.28	87.54	16.35	14.73
	Lessmann N. [22]	85.08	94.25	8.58	4.62	85.76	93.86	8.20	5.38
	nnUNet [15]	85.81	92.55	12.50	10.25	86.59	92.62	12.78	12.00
	Verteformer [45]	86.39	91.22	11.14	10.28	86.54	90.74	10.55	10.51
	UNeXt [39]	83.80	85.20	18.63	13.51	83.36	88.39	12.19	11.77
	Swin UNETR [37]	85.42	90.57	16.01	12.55	83.46	88.91	16.03	13.58
	MedNeXt [32]	88.51	93.96	10.59	8.47	88.91	94.40	11.35	9.81
Multi-stage	Sekuboyina A. [34]	83.06	90.93	12.11	7.56	83.18	92.79	9.94	7.22
Multi-stage	Payer C. [31]	90.90	95.54	6.35	4.62	89.80	95.47	7.08	4.45
Two-stage	Tao R. [38]	90.49	94.26	6.53	4.31	89.94	94.01	6.96	4.73
Two-stage	Ours	92.17	95.62	5.91	4.06	91.33	96.03	5.97	4.27

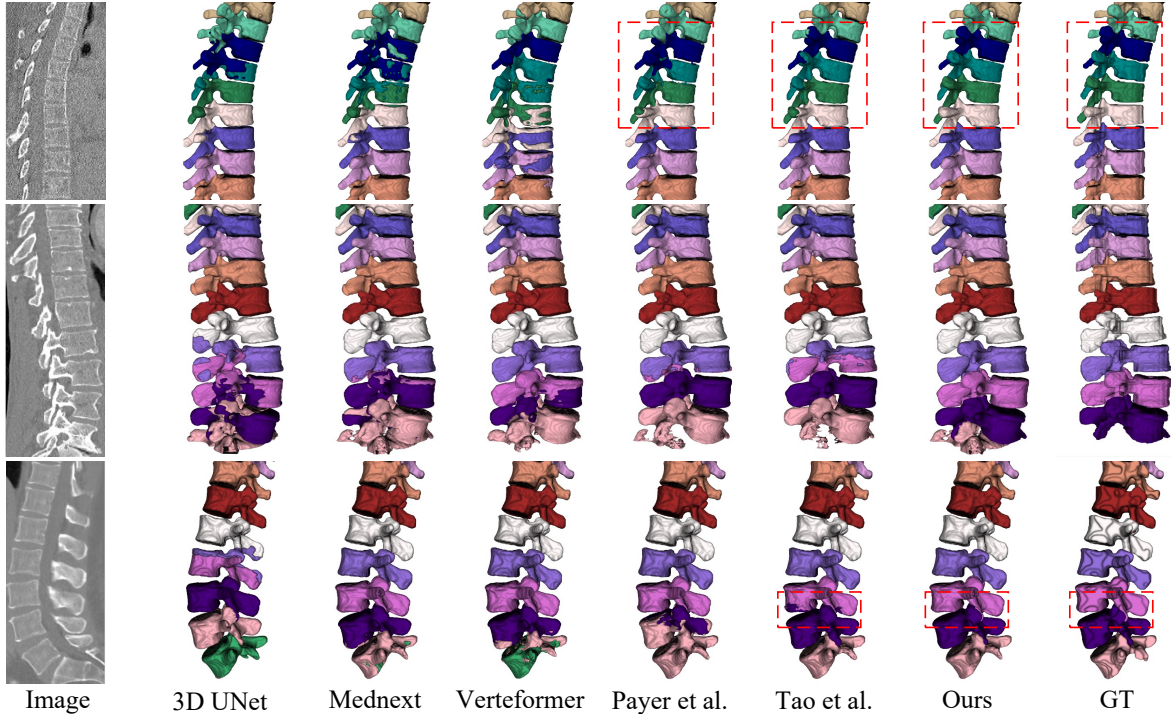


Fig. 6. Qualitative visualizations of hard cases by single-stage, two-stage, and multi-stage models in the benchmark. The 1st row: a case from VerSe 2019. The 2nd and 3rd row: two cases from VerSe 2020.

scans for training, public test, and hidden test cases. VerSe 2020 is a more challenging dataset, containing more CT scans with pathological appearances, fractures, and metal artifacts. We follow the standard data-split setting, with 89/103/103 scans for training, public test, and hidden test cases.

To ensure relatively fixed FOVs of iterative cropped patches in the second stage, we resample all data with a voxel space equal to $1 \times 1 \times 1.998mm^3$ and $0.8262 \times 0.8262 \times 1mm^3$ for VerSe 2019 and 2020 respectively. Then we crop patches containing at least three sequential vertebrae, with the patch size equal to $112 \times 128 \times 64$ and $128 \times 128 \times 96$. Each patch is centered at the spherical centroid of the intermediate vertebra. A random translation is exerted on the patch center to generate the variance in the center regression decoder, with a $[-5, 5]$ range on each coordinate axis. For each middle vertebra, we repeat the translation process 3 times. To further simulate

various types of imprecise boundary prediction, different pre-trained weights are adopted to generate coarse predictions for the positional prompt. For VerSe 2019, a total of 7767 patches from 80 training CT scans are split as 6214/1553 cases for training and validation. For VerSe 2020, following the same 4:1 ratio, 10188 patches are split as 8150/2038 cases. During inference, the SLoRD framework is adopted to refine coarse predictions. Moreover, Dice score and Hausdorff distance (HD) are chosen as quantitative metrics [44].

Implementation Details. All experiments are implemented based on Pytorch and trained on 2 NVIDIA Tesla V100 GPUs. In stage 1, MedNeXt [32] is selected as the U-shape backbone with large receptive fields to extract long-term semantics, trained for 1000 epochs with 10.53M parameters. And we utilize a combination of cross entropy loss and Dice loss followed by [15]. The patch size is $128 \times 160 \times 96$. In stage 2,

TABLE II

COMPARISONS WITH OTHER SINGLE-STAGE, TWO-STAGE, AND MULTI-STAGE METHODS ON THE PUBLIC AND HIDDEN TEST DATASETS OF VERSE 2020 (A-DICE: AVERAGE DICE. M-DICE: MEDIAN DICE. A-HD: AVERAGE HAUSDORFF DISTANCE. M-HD: MEDIAN HAUSDORFF DISTANCE).

Stage	Method	Public test				Hidden test			
		A-Dice \uparrow	M-Dice \uparrow	A-HD \downarrow	M-HD \downarrow	A-Dice \uparrow	M-Dice \uparrow	A-HD \downarrow	M-HD \downarrow
Single-stage	3D UNet [11]	82.69	89.49	11.15	9.40	83.32	88.90	10.59	9.02
	Xiangshang Z. [34]	83.58	92.69	15.19	9.76	85.07	93.29	12.99	8.44
	nnUNet [15]	85.34	92.10	10.01	8.47	86.83	91.79	9.29	7.58
	Verteformer [45]	85.44	92.04	9.19	8.86	86.57	91.47	9.80	8.23
	UNeXt [39]	81.19	90.30	13.39	11.94	82.77	87.94	12.39	12.72
	Swin UNETR [37]	82.57	90.68	12.07	10.16	81.83	88.79	12.98	11.37
	MedNeXt [32]	87.35	93.26	8.98	7.50	87.75	92.41	8.31	6.28
Multi-stage	Sekuboyina A. [34]	78.05	85.09	10.99	6.38	79.52	85.49	11.61	7.76
Two-stage	Yeah T. [34]	88.88	92.93	9.57	5.43	87.91	92.76	8.41	5.91
Multi-stage	Payer C. [31]	91.65	<u>95.72</u>	<u>5.80</u>	<u>4.06</u>	89.71	95.65	<u>6.06</u>	<u>3.94</u>
Multi-stage	Chen D. [34]	91.72	95.52	6.14	4.22	91.23	95.21	7.15	4.30
Two-stage	Tao R. [38]	91.29	95.33	6.30	4.73	<u>91.65</u>	94.72	6.29	5.07
Two-stage	Ours	92.09	95.75	5.30	3.78	92.31	<u>95.33</u>	5.55	3.74

SLoRD is trained for 400 epochs, which employs the encoder of 3D UNet with only 5.15M parameters. And we utilize a weighted loss \mathcal{L}_{total} as illustrated in Section III-C. We train all models using AdamW optimizer. With the linear warm-up strategy, the initial learning rate is set as $5e-4$ with a cosine learning rate decay scheduler, and weight decay is set as $1e-5$. The batch size is 2 and 16 for two stages individually. The hyperparameters s (sampling interval) and k (number of basic contour descriptors) are set as 5° and 200 for a better trade-off between performance and efficiency.

B. Performance Comparison

1) *VerSe 2019*: To evaluate the efficacy of SLoRD, quantitative experimental results are first conducted on VerSe 2019. As illustrated by Table I, our method achieves SOTA performance on the average Dice and Hausdorff distance (HD) of the hidden test dataset compared with other single-stage, two-stage, and multi-stage methods. Specifically, our framework surpasses MedNeXt [32] (the best single-stage model) by 2.42% \uparrow average Dice score and 5.38mm \downarrow average Hausdorff distance. And these two metrics come to 1.39% \uparrow and 0.99mm \downarrow when compared with Spine-Transformer [38] (the strongest two-stage model), 1.53% \uparrow and 1.11mm \downarrow compared with Payer’s method [34] (the powerful multi-stage model). Moreover, the median Dice and HD of our method also reach a quite promising performance.

2) *VerSe 2020*: To further validate the robustness and universality of SLoRD, we carry out a quantitative analysis on VerSe 2020, which contains more challenging cases with deformed shapes and metal artifacts. As shown in Table II, our approach achieves the best boundary delineation results with the lowest average HD values. Compared with Chen’s method [34], 0.84mm \downarrow and 1.60mm \downarrow Hausdorff distance are acquired for the public and hidden test datasets. Also, the median HD values reveal our method could improve the segmentation performance for not only satisfactory cases but poor cases. Obviously, the superior segmentation performance originates from the strict voxel consistency and contour precision regularization generated from the instance-based SLoRD

TABLE III

THE MODEL EFFICIENCY EVALUATION BETWEEN OUR METHOD AND OTHER APPROACHES ON THE HIDDEN TEST DATASETS OF VERSE 2019.

Method	Parameters (M)	FLOPs (G)	Inference speed (s)
Verteformer [45]	330.65	336.5	65.2
Payer C. [31]	34.33	517.6	260.0
Tao R. [38]	38.41	631.3	176.3
Ours	25.18	454.6	142.8

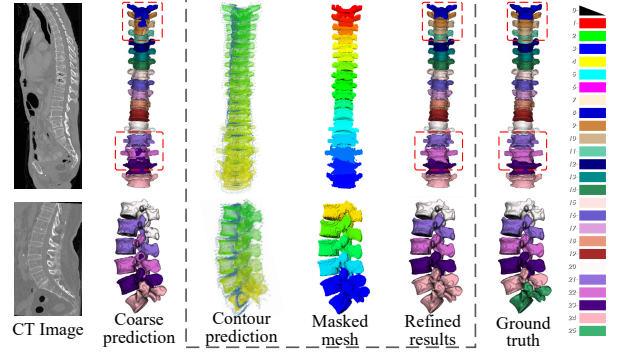


Fig. 7. Visualizations of the detailed refinement process. Refined predictions in the dashed box reveal a better segmentation consistency in each vertebra compared with coarse predictions.

architecture. By labeling sequential instance masks, we will acquire semantic masks with better consistency.

3) *Qualitative results*: Qualitative visualizations of some challenging cases are displayed in Fig. 6. The first case visualizes thoracic vertebrae with similar shapes. Besides, the spinous process of the precedent vertebra shows the same height as the superior articular process and vertebral body of the latter vertebra, prone to imprecise boundary predictions. The second case is plagued by metal artifacts, making it difficult to identify and locate several vertebrae in the bottom. The third case illustrates the potential problem of inter-class boundary confusion between normal vertebrae and transitional vertebrae [34]. And our method can better address the above obstacle with intra-vertebrae segmentation consistency.

For a detailed mask refinement process, intermediate results

TABLE IV

ABLATION STUDY ON THE ORIENTATION OF POSITIVE Z-AXIS, SAMPLING INTERVAL, AND THE NUMBER OF BASIC CONTOUR DESCRIPTORS (ASD [44]: AVERAGE SURFACE DISTANCE).

(a) Ablation on the choice of positive Z-axis			
Settings	x-axis	y-axis	z-axis
ASD ↓	0.987±0.074	1.189±0.114	0.962±0.073
(b) Ablation on the sampling interval			
Settings	3°	5°	10°
ASD ↓	0.876±0.067	0.962±0.073	1.245±0.122
(c) Ablation on the rank number			
Settings	100	200	500
ASD ↓	1.033±0.080	0.962±0.073	0.917±0.068

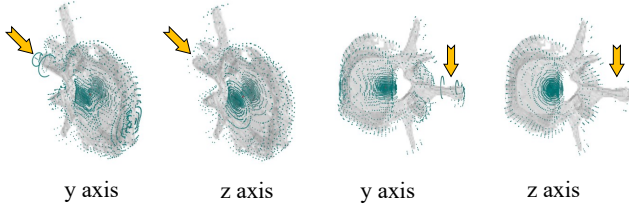


Fig. 8. Visualizations of the full-rank contour restoration on the orientation setting of positive Z-axis in the spherical coordinate system. The voxel z axis from inferior to superior orientations is chosen as the final experimental setting.

are provided in Fig. 7. Given coarse predictions in stage 1, SLoRD will generate contour predictions for each vertebra. Then discrete contour point clouds are transformed into a sequence of masked meshes. After filling the inner volume, refined masks will be attained with good boundary precision for each class as shown in the dashed box of Fig. 7. SLoRD can function well as long as the top two vertebrae perform satisfactorily, even with moderate inconsistency. It is worth highlighting that each instance mask is generated via the linear combination of basic contour descriptors, which can be acquired by SVD offline. A depiction of decomposed contour priors can be referred to in Fig. 3.

4) *Model Efficiency*: Besides, the efficiency analysis is conducted between our framework and other typical methods on the hidden test dataset of VerSe 2019. Specifically, we choose model parameters, computational costs, and inference time per case as quantitative metrics. As illustrated by Table III, our approach only requires 25.18M network parameters, which is the most lightweight model in the referenced methods. Besides, our approach achieves a 142.8s average inference time for each CT scan, much faster than Payer’s method (260.0s) and Tao’s method (176.3s).

C. Discussion

1) Settings for the spherical-based contour representations:

We investigate a detailed ablation analysis on the contour representations based on the spherical coordinate system. For a simple yet effective evaluation, we adopt the average surface distance (ASD) between contour points and the boundary to assess the contour restoration performance. The ASD value in Table IV is calculated via the linear combination of full-rank contour descriptors from SVD. Thus, this distance value stands

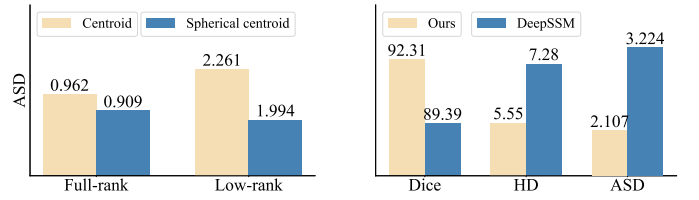


Fig. 9. Left: ablation study on the type of centers between the centroid and spherical center (ASD [44]: average surface distance). Right: performance comparison between our method and DeepSSM on VerSe 2020.

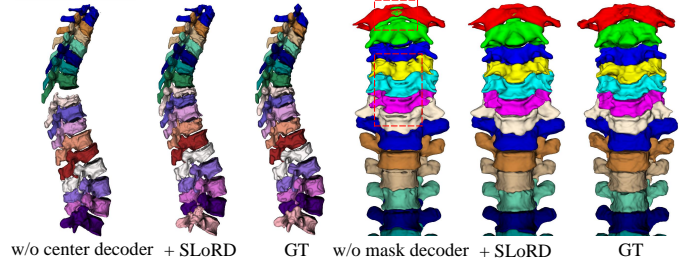


Fig. 10. Qualitative results for the ablation study on the center decoder and mask decoder of SLoRD.

for the best performance that can be theoretically achieved due to vertebral non-convex shape property and deviation due to integer approximation.

The orientation of the positive Z-axis in the spherical coordinate system: As revealed in Table IV, the voxel z-axis as the objective orientation achieves the lowest ASD value. Compared with the voxel x-axis, there is a 0.227 voxel distance drop. Besides, as revealed in Fig. 8, there will be a deviation for contour points adjacent to the spinous process of vertebrae when comparing the setting of z-axis with y-axis.

Sampling interval of the azimuth angle ϕ and the polar angle θ : Different values of the angular interval are also considered. As shown in Table IV, a smaller interval means a denser sampling for the contour point cloud, which will promote the precision of regressed contours by SLoRD, and then elevate the final segmentation performance. However, that behavior will inevitably bring heavier computational costs. Considering the balance, that hyper-parameter is specified as 5° , then the dimension N of each contour descriptor ρ is equal to $\frac{360^\circ}{5^\circ} \times (\frac{180^\circ}{5^\circ} + 1) = 2664$.

The rank of basic contour descriptors: According to Table IV, 200 basic contour descriptors can already restore the original contour with sufficient precision. That is also proven in the qualitative results of Fig. 3.

Spherical centroid vs. Centroid: Adopting the spherical centroid reduces the ASD value in both low-rank and full-rank approximations, with a 0.053 ↓ and 0.267 ↓ respectively as shown in Fig. 9. That demonstrates the advancement of spherical centroids owing to the distance-based optimization objective between contour points and the vertebral surface.

2) *Structural ablation on SLoRD*: Furthermore, we conduct the structural ablation analysis for SLoRD on VerSe 2020.

Coefficient decoder: Without the coefficient decoder, contours cannot be generated. Thus, that is the essential part. For the reason why the regression of contour points is not

TABLE V
ABLATION STUDY ON THE COMBINATION OF DECODERS ON VERSE 2020.

Method	Dice score (%) \uparrow					HD (mm) \downarrow				
	Cervical	Thoracic	Lumbar	Mean	Median	Cervical	Thoracic	Lumbar	Mean	Median
Ours	90.27	93.44	90.69	92.31	95.33	6.37	4.68	6.04	5.55	3.74
w/o mask decoder	87.82	90.32	88.38	90.13	94.47	8.00	6.87	7.07	7.29	5.86
w/o coefficient decoder	-	-	-	-	-	-	-	-	-	-
w/o center decoder	87.41	90.50	85.96	88.64	93.80	8.13	6.14	9.11	8.09	6.75
w/o positional prompts	89.58	89.83	89.62	91.22	94.85	6.86	7.09	6.19	6.63	5.03

TABLE VI

ABLATION STUDY ON THE PLUG-AND-PLAY PROPERTY OF SLoRD WHEN APPLIED TO OTHER SINGLE-STAGE, TWO-STAGE, AND MULTI-STAGE METHODS ON VERTEBRAE SEGMENTATION. QUANTITATIVE RESULTS ON THE HIDDEN TEST DATASET OF VERSE 2019 AND 2020.

VerSe 2019				
Methods	A-Dice	M-Dice	A-HD	M-HD
Verteformer [45]	86.54	90.74	10.55	10.51
Verteformer [45] + SLoRD	89.34	92.98	6.73	6.31
Payer C. [31]	89.80	95.47	7.08	4.45
Payer C. [31] + SLoRD	90.97	95.26	5.93	4.28
Tao R. [38]	89.94	94.01	6.96	4.73
Tao R. [38] + SLoRD	91.46	95.72	5.73	4.23
VerSe 2020				
Verteformer [45]	86.57	91.47	9.80	8.23
Verteformer [45] + SLoRD	89.22	93.90	7.64	5.55
Payer C. [31]	89.71	95.65	6.06	3.94
Payer C. [31] + SLoRD	91.72	95.73	5.58	4.08
Tao R. [38]	91.65	94.72	6.29	5.07
Tao R. [38] + SLoRD	92.24	95.11	5.27	4.34

performed directly in this part, we reckon that models show deficient abilities to perceive and localize contour points with the specific angle. Therefore, basic contour descriptors with latent angular information serve as strong guidance to generate target contour points.

Mask decoder: Without it, SLoRD reveals degraded segmentation performance, with a 2.18% \downarrow average Dice score according to Table V. Carrying out the cause and effect analysis, this mask decoder will bring additional shape information, which boosts the contour restoration precision according to Eq (3). For more detailed evaluations, the missing of this component will affect the boundary delineation for cervical vertebrae as shown in Fig.10.

Center decoder: Since the coupling effects between spherical centers and coefficients, removing the center decoder will diminish the segmentation performance significantly, with 3.67% \downarrow average Dice score and 3.07mm \uparrow average HD. Besides, as portrayed in Fig.10, there exists a missing detection for a specific vertebra, resulting in sequential identification errors. That phenomenon significantly weakens segmentation results on lumbar vertebrae [8].

Positional prompts: The positional priors promote the regression for spherical centroids, further boost the precision of contour generation. This detection guidance is beneficial to segment the thoracic region with adjacent vertebrae.

3) Plug-and-play: We also carried out the ablation study on the plug-and-play property of SLoRD on VerSe 2019 and 2020. Besides MedNeXt [32], the proposed SLoRD will boost segmentation results achieved by Verteformer [45], Spine-Transformer [38], Payer's method [31] as shown in Table

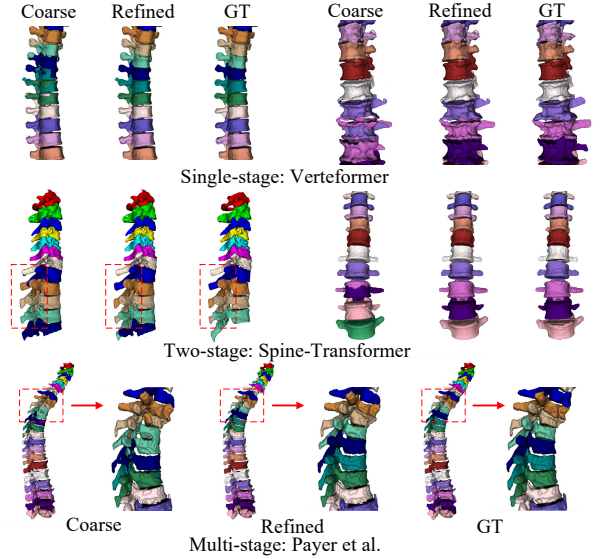


Fig. 11. Improvement of our proposed SLoRD when applied to coarse predictions from other segmentation networks including the single-stage Verteformer [45], two-stage Spine-Transformer [38], and multi-stage Payer's method [31].

VI. Specifically, for Verteformer on VerSe 2020, substantial improvements have been achieved on the average Dice score and HD (2.65% \uparrow , 2.16mm \downarrow). Also, SLoRD can repair segmentation results by Payer's approach, with 2.01% \uparrow average Dice score and 0.48mm \downarrow average HD. Qualitative results are provided in Fig.11 to demonstrate the efficacy of SLoRD in promoting segmentation consistency when plugged into single-stage, two-stage, and multi-stage methods.

4) Comparison with PCA-based shape model: As we mentioned in Section III-A, SVD shows the best low-rank approximation property and can mine more robust shape descriptors compared with PCA. Here a straight comparison is implemented on the hidden test dataset of VerSe 2020. As illustrated in Table 9, our method outperforms DeepSSM significantly, with a 3.92% higher Dice score and a 1.73mm lower Hausdorff distance. Also, since different vertebrae bear various numbers of contour points, it is tricky to carry out the uniform sampling process while delineating the original contour. In contrast, our method achieves a 1.117 \downarrow ASD value, showing more satisfactory contour reconstruction results based on the structural encoding way of contour representations.

V. CONCLUSION

In this paper, to address the challenge of intra-vertebrae segmentation inconsistency, we devise SLoRD by jointly impos-

ing voxel consistency and contour precision regularizations. Specifically, we propose a structural contour representation way based on the spherical coordinate system. Besides, basic contour descriptors and shape constraints facilitate regressed contour points close to vertebral surfaces. Detailed quantitative and qualitative results on VerSe 2019 and 2020 demonstrate the superiority of our method compared with other single-stage, two-stage and multi-stage models. Moreover, SLoRD serves as a plug-and-play framework to repair the segmentation in-consistency in coarse predictions from other methods.

REFERENCES

- [1] S. M. R. Al Arif, K. Knapp, and G. Slabaugh. Fully automatic cervical vertebrae segmentation framework for x-ray images. *Computer methods and programs in biomedicine*, 157:95–111, 2018.
- [2] S. M. R. Al Arif, K. Knapp, and G. Slabaugh. Spnet: Shape prediction using a fully convolutional neural network. In *MICCAI*, pages 430–439. Springer, 2018.
- [3] M. S. Aslan, A. Ali, et al. 3d vertebrae segmentation using graph cuts with shape prior constraints. In *ICIP*, pages 2193–2196. IEEE, 2010.
- [4] R. Bhalodia, S. Elhabian, J. Adams, W. Tao, L. Kavan, and R. Whitaker. Deepssm: A blueprint for image-to-shape deep learning models. *Medical Image Analysis*, 91:103034, 2024.
- [5] J. E. Burns, J. Yao, et al. Automated detection, localization, and classification of traumatic vertebral body fractures in the thoracic and lumbar spine at ct. *Radiology*, 278(1):64–73, 2016.
- [6] H. Chang, S. Zhao, H. Zheng, Y. Chen, and S. Li. Multi-vertebrae segmentation from arbitrary spine mr images under global view. In *MICCAI*, pages 702–711. Springer, 2020.
- [7] D. Chen, Y. Bai, et al. Deep reasoning networks for unsupervised pattern de-mixing with constraint reasoning. In *ICML*, pages 1500–1509. PMLR, 2020.
- [8] Y. Chen, Y. Gao, et al. Vertebrae identification and localization utilizing fully convolutional networks and a hidden markov model. *IEEE Transactions on Medical Imaging*, 39(2):387–399, 2019.
- [9] J. C. Cheng, R. M. Castelein, et al. Adolescent idiopathic scoliosis. *Nature reviews disease primers*, 1(1):1–21, 2015.
- [10] C. Chu, D. L. Belavý, et al. Fully automatic localization and segmentation of 3d vertebral bodies from ct/mr images via a learning-based method. *PloS one*, 10(11):e0143327, 2015.
- [11] Ö. Çiçek, A. Abdulkadir, S. S. Lienkamp, T. Brox, and O. Ronneberger. 3d u-net: learning dense volumetric segmentation from sparse annotation. In *MICCAI*, pages 424–432. Springer, 2016.
- [12] A. Dosovitskiy, L. Beyer, A. Kolesnikov, et al. An image is worth 16x16 words: Transformers for image recognition at scale. In *International Conference on Learning Representations*, 2021.
- [13] M.-A. Gafencu, Y. Velikova, M. Saleh, T. Ungi, N. Navab, et al. Shape completion in the dark: completing vertebrae morphology from 3d ultrasound. *IJCARS*, pages 1–9, 2024.
- [14] K. Hammernik, T. Ebner, D. Stern, M. Urschler, and T. Pock. Vertebrae segmentation in 3d ct images based on a variational framework. *Recent advances in computational methods and clinical applications for spine imaging*, pages 227–233, 2015.
- [15] F. Isensee, P. F. Jaeger, S. A. Kohl, J. Petersen, and K. H. Maier-Hein. nnu-net: a self-configuring method for deep learning-based biomedical image segmentation. *Nature methods*, 18(2):203–211, 2021.
- [16] R. Janssens, G. Zeng, et al. Fully automatic segmentation of lumbar vertebrae from ct images using cascaded 3d fully convolutional networks. In *ISBI*, pages 893–897. IEEE, 2018.
- [17] S. Kadoury, H. Labelle, and N. Paragios. Automatic inference of articulated spine models in ct images using high-order markov random fields. *Medical image analysis*, 15(4):426–437, 2011.
- [18] S. Kadoury, H. Labelle, and N. Paragios. Spine segmentation in medical images using manifold embeddings and higher-order mrfs. *IEEE transactions on medical imaging*, 32(7):1227–1238, 2013.
- [19] B. M. Kelm et al. Spine detection in ct and mr using iterated marginal space learning. *Medical image analysis*, 17(8):1283–1292, 2013.
- [20] T. Klinder, J. Ostermann, M. Ehm, A. Franz, R. Kneser, and C. Lorenz. Automated model-based vertebra detection, identification, and segmentation in ct images. *Medical image analysis*, 13(3):471–482, 2009.
- [21] D. Knez, B. Likar, F. Pernuš, and T. Vrtovec. Computer-assisted screw size and insertion trajectory planning for pedicle screw placement surgery. *IEEE transactions on medical imaging*, 35(6):1420–1430, 2016.
- [22] N. Lessmann et al. Iterative fully convolutional neural networks for automatic vertebra segmentation and identification. *Medical image analysis*, 53:142–155, 2019.
- [23] P. H. Lim, U. Bagci, and L. Bai. A robust segmentation framework for spine trauma diagnosis. In *Computational Methods and Clinical Applications for Spine Imaging: Proceedings of the Workshop held on MICCAI, 2013, Japan*, pages 25–33. Springer, 2014.
- [24] M. T. Löffler, A. Sekuboyina, A. Jacob, A.-L. Grau, et al. A vertebral segmentation dataset with fracture grading. *Radiology: Artificial Intelligence*, 2(4):e190138, 2020.
- [25] W. E. Lorensen and H. E. Cline. Marching cubes: A high resolution 3d surface construction algorithm. In *Seminal graphics: pioneering efforts that shaped the field*, pages 347–353. 1998.
- [26] N. Masuzawa, Y. Kitamura, et al. Automatic segmentation, localization, and identification of vertebrae in 3d ct images using cascaded convolutional neural networks. In *MICCAI*, pages 681–690. Springer, 2020.
- [27] D. Meng, E. Boyer, et al. Vertebrae localization, segmentation and identification using a graph optimization and an anatomic consistency cycle. *Computerized Medical Imaging and Graphics*, 107:102235, 2023.
- [28] H. Möller, R. Graf, J. Schmitt, et al. Spineps-automatic whole spine segmentation of t2-weighted mr images using a two-phase approach to multi-class semantic and instance segmentation. *arXiv preprint arXiv:2402.16368*, 2024.
- [29] S. Pang, C. Pang, et al. Spineparsenet: spine parsing for volumetric mr image by a two-stage segmentation framework with semantic image representation. *IEEE TMI*, 40(1):262–273, 2020.
- [30] W. Park, D. Jin, and C.-S. Kim. Eigencontours: Novel contour descriptors based on low-rank approximation. In *CVPR*, pages 2667–2675, 2022.
- [31] C. Payer, D. Stern, H. Bischof, and M. Urschler. Coarse to fine vertebrae localization and segmentation with spatialconfiguration-net and u-net. In *VISIGRAPP (5: VISAPP)*, pages 124–133, 2020.
- [32] S. Roy, G. Koehler, C. Ulrich, M. Baumgartner, J. Petersen, F. Isensee, P. F. Jaeger, and K. H. Maier-Hein. Mednext: transformer-driven scaling of convnets for medical image segmentation. In *MICCAI*, pages 405–415. Springer, 2023.
- [33] W. Schroeder, K. M. Martin, and W. E. Lorensen. *The visualization toolkit an object-oriented approach to 3D graphics*. Prentice-Hall, Inc., 1998.
- [34] A. Sekuboyina, M. E. Husseini, et al. Verse: a vertebrae labelling and segmentation benchmark for multi-detector ct images. *Medical image analysis*, 73:102166, 2021.
- [35] A. Sekuboyina, M. Rempfler, J. Kukačka, G. Tetteh, et al. Btrfly net: Vertebrae labelling with energy-based adversarial learning of local spine prior. In *MICCAI*, pages 649–657. Springer, 2018.
- [36] A. Sekuboyina, A. Valentinitich, J. S. Kirschke, and B. H. Menze. A localisation-segmentation approach for multi-label annotation of lumbar vertebrae using deep nets. *arXiv preprint arXiv:1703.04347*, 2017.
- [37] Y. Tang, D. Yang, W. Li, H. R. Roth, B. Landman, D. Xu, V. Nath, and A. Hatamizadeh. Self-supervised pre-training of swin transformers for 3d medical image analysis. In *CVPR*, pages 20730–20740, 2022.
- [38] R. Tao, W. Liu, and G. Zheng. Spine-transformers: Vertebra labeling and segmentation in arbitrary field-of-view spine cts via 3d transformers. *Medical Image Analysis*, 75:102258, 2022.
- [39] J. M. J. Valanarasu et al. Unext: Mlp-based rapid medical image segmentation network. In *MICCAI*, pages 23–33. Springer, 2022.
- [40] M. E. Wall, A. Rechtsteiner, and L. M. Rocha. Singular value decomposition and principal component analysis. In *A practical approach to microarray data analysis*, pages 91–109. Springer, 2003.
- [41] E. W. Weisstein. Spherical coordinates. <https://mathworld.wolfram.com/>, 2005.
- [42] H. Wu, J. Zhang, Y. Fang, Z. Liu, N. Wang, Z. Cui, and D. Shen. Multi-view vertebra localization and identification from ct images. In *International Conference on Medical Image Computing and Computer-Assisted Intervention*, pages 136–145. Springer, 2023.
- [43] E. Xie, P. Sun, X. Song, W. Wang, X. Liu, D. Liang, C. Shen, and P. Luo. Polarmask: Single shot instance segmentation with polar representation. In *CVPR*, pages 12193–12202, 2020.
- [44] V. Yeghiazaryan and I. Voiculescu. Family of boundary overlap metrics for the evaluation of medical image segmentation. *Journal of Medical Imaging*, 5(1):015006–015006, 2018.
- [45] X. You, Y. Gu, et al. Verteformer: A single-staged transformer network for vertebrae segmentation from ct images with arbitrary field of views. *Medical Physics*, 2023.
- [46] X. You, Y. Gu, Y. Liu, et al. Eg-trans3dunet: a single-staged transformer-based model for accurate vertebrae segmentation from spinal ct images. In *ISBI*, pages 1–5. IEEE, 2022.